Study of Central Exclusive Production of $\pi^+\pi^-$, K^+K^- and $p\bar{p}$ Pairs in Proton-Proton Collisions at $\sqrt{s} = 510$ GeV with the STAR detector at RHIC

The STAR Collaboration

E-mail: Tomas.Truhlar@fjfi.cvut.cz

ABSTRACT: We report on the measurement of the $pp \rightarrow ph^+h^-p$ ($h = \pi, K, p$) central exclusive production process in proton-proton collisions at the center-of-mass energy $\sqrt{s} = $ 510 GeV with the STAR detector at RHIC. At this energy, the process is dominated by a double $\mathbb{P}$omeron exchange mechanism. The oppositely charged hadron pairs are measured within the central detector of STAR, the Time Projection Chamber, and the Time of Flight detector. The hadron pairs are identified using the ionization energy loss and the time of flight method. The forward scattered protons, which remain intact inside the RHIC beam pipe after the collision, are measured in the Roman Pot system allowing the verification of the event's exclusivity. Differential fiducial cross sections within the STAR acceptance are presented as function of the difference in the azimuthal angle between the outgoing protons, hadron pair invariant mass, and rapidity of the central system. The centrally produced hadrons are measured within the STAR acceptance in the pseudorapidity range $|\eta| < 0.9$. The invariant masses of the charged hadrons pairs are measured up to approximately 3 GeV and the square of the four-momentum transfer (t_1 and t_2) of the two forward-scattered protons is in the range 0.3 GeV$^2 < -t_1, -t_2 < 1.6$ GeV^2. The differential fiducial cross sections of the forward protons as a function of the $|t_1 + t_2|$ are also presented. All results for the $\pi^+\pi^-$ pair are presented in three mass ranges. A comparison with GRANIITTI Monte Carlo predictions are also presented, where the spectra include continuum and resonant contributions.

Contents

1 Introduction

Measurement of Central Exclusive Production (CEP) of charged hadron pairs in the Double IPomeron Exchange (DIPE) process [1] provides a unique opportunity to study quantum chromodynamics (QCD), the theory of strong interaction. The validity of QCD has been demonstrated in many experiments since the 1970s, in particular at hadron colliders, like the measurements of CEP at the Intersecting Storage Rings (ISR) by the AFS [2] experiment, at RHIC by the STAR [3] experiment, and at the Large Hadron Collider (LHC) by the CMS [4] experiment, and also by the measurement of central production at the Tevatron by the CDF [5] experiment.

In this paper, we present the results on CEP in DIPE. They probe the non-perturbative regime of QCD where Regge theory is often used to describe such interactions. In QCD, the IPomeron is modeled as a color-singlet object, carrying no net color charge. In the lowest

order, it can be represented as a two-gluon exchange in a color-neutral configuration. As no color is exchanged in DIPE, the color content of each proton is preserved allowing both protons to stay intact after the collision. The presence of large rapidity gaps between the centrally produced system and the outgoing protons is a key signature of such events.

These features make DIPE an ideal process for exploring the structure of the IPomeron and the non-perturbative aspects of QCD. However, theoretical non-perturbative approaches [6, 7] remain challenging due to the theoretical complexity of the process, which involves significant interference between resonant and continuum production, as well as re-scattering effects via additional interaction between the protons. Moreover, the charged hadron pairs produced in DIPE are constrained to quantum numbers: $I^G J^{PC} = 0^+(even)^{++}$. This constraint acts as a "quantum number filter" making DIPE a powerful tool for meson spectroscopy, particularly for identifying glue-rich states. In addition, such measurements provide valuable insight into the internal structure and behavior of the IPomeron itself [8], absorption effects [9, 10], and factorization breaking [11] between the two proton vertices especially thanks to measurement of forward-scattered protons. Furthermore, the DIPE provides a gluon-rich environment suitable to study production of glueballs [12], bound states of gluons. The experimental confirmation of the glueball existence would be yet another strong support for the validity of QCD. However, the exact nature of the IPomeron still remains elusive and the existence of a glueball has not been unambiguously confirmed yet, despite its theoretical predictions.

Figure 1 shows diagrams of production h^+h^- pairs, where h^+h^- are $\pi^+\pi^-$, K^+K^-, and $p\bar{p}$, in the DIPE process, in non-perturbative QCD regime: central exclusive resonant production (left) and continuum (non-resonant) production (middle). Also, representation of continuum production within perturbative QCD is shown in the two-gluon approximation model (right).
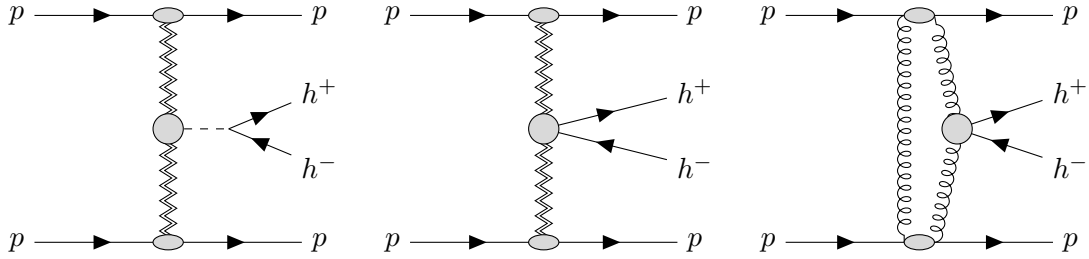

Figure 1. Diagrams of CEP of h^+h^- in DIPE process. The resonant (left) and continuum production (middle) are shown. The two-gluon approximation of continuum production in DIPE in perturbative QCD (right) is also shown. IPomerons are represented by double zigzag lines and gluons by spiral lines. The vertices are drown by gray circles to indicate non-perturbative interactions.

By its nature CEP is a process where colliding protons stay intact after the collision. The outgoing intact protons are detected using detectors placed in special vessels called Roman Pots. The recoil system, which is well separated from the forward-scattered protons by rapidity gaps, characteristic of DIPE, is produced in the center of rapidity. It is measured

in the Time Projection Chamber (TPC) and in the Time of Flight (TOF) systems. The rapidity gaps $2.1 < |\eta| < 5.0$ are ensured by a vetoes in the the Beam-Beam Counters (BBC). The adjective "exclusive" means that all particles in the final state are measured. This gives us full control of the interaction's kinematics and verification of its exclusivity.

This paper presents a measurement of $\pi^+\pi^-$, K^+K^-, and $p\bar{p}$ in CEP process in proton-proton collisions at $\sqrt{s} = 510$ GeV with the STAR detector at the Relativistic Heavy Ion Collider (RHIC) [13, 14].

Differential and integrated cross sections are measured within the STAR detector's acceptance. The results are compared with the previous STAR results on CEP of charged hadron pairs in proton-proton collisions at $\sqrt{s} = 200$ GeV [3]. Throughout the paper, the natural units $c = \hbar = 1$ are used.

2 Experimental setup

This measurement utilizes various subsystems of the STAR experiment in a configuration similar to that used for the CEP measurements in proton-proton collisions at $\sqrt{s} = 200$ GeV [3]. The parts of the setup relevant to this analysis are presented below.

Solenoidal Tracker at RHIC (STAR), is a general-purpose detector at RHIC, with 0.5 Tesla [15] solenoidal magnetic field parallel to the beam axis. RHIC is a versatile collider with two main programs: collisions of relativistic heavy ions and polarized protons with $\sqrt{s}$ up to 510 GeV. It has full azimuthal coverage $0 < \varphi < 2\pi$, and pseudorapidity coverage $|\eta| < 1.0$ for charged particle detection and identification, which allows to perform this measurement[1]. Figure 2 shows the STAR detector with its sub-detectors, namely TPC [16], TOF [17], BBC [18], the Vertex Position Detector (VPD) [19], and the Barrel Electromagnetic Calorimeter (BEMC). Furthermore, the STAR experiment includes forward systems: the Zero-Degree Calorimeters (ZDC) [20, 21] and the Roman Pot (RP) system [22]. These sub-detectors are located down the beam line and they are particularly important for the CEP analysis, especially the RP system. In the following the sub-detectors are briefly described.

The TPC is a gaseous detector, which provides both tracking information and an average ionization energy loss per unit length ($\langle dE/dx \rangle$) for each track. The momentum reconstruction and the $\langle dE/dx \rangle$ allow identification of charged hadrons: pions, kaons, and protons. It has cylindrical shape with the length of 4.2 m, the inner radius of 0.5 m and the outer radius of 2 m. The TPC has full azimuthal coverage and pseudorapidity coverage $|\eta| < 1.0$.

The TOF system is a cylindrical detector around the TPC extending the particle identification (PID) capabilities of the TPC for particles with momenta up to ~ 3 GeV. The TOF is composed of adjacent Multi-gap Resistive Plate Chambers covering full azimuthal angle and the pseudorapidity $|\eta| < 0.9$. It is a fast timing detector with a time resolution between $60 - 100$ ps. Therefore, it is often used to trigger on charged particle multiplicity

---

[1]The origin is at the interaction point (IP) at the center of the detector. The z-axis is aligned with the center of the beam pipe, the x-axis points outward from the IP toward the outside of the RHIC ring, and the y-axis points upward. The pseudorapidity η is defined in terms of the polar angle θ as $\eta = -\ln\left(\tan\left(\frac{\theta}{2}\right)\right)$.
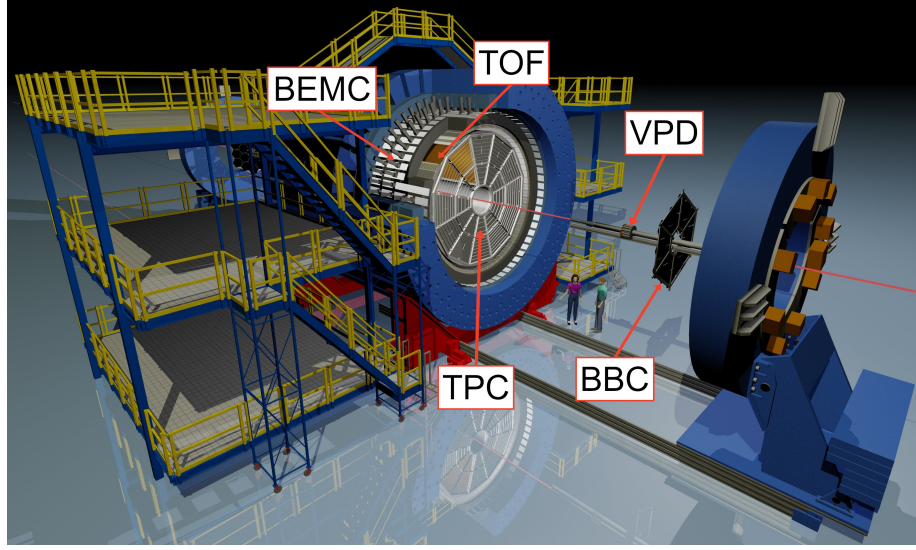
Figure 2. The schematic view of the STAR experiment. Main sub-detectors, including the TPC, the TOF, the BBC, the VPD and the BEMC are highlighted.

in the central rapidity. For the CEP events, it is crucial for triggering on low multiplicity events in the TPC. Moreover, it helps to discriminate in-time TPC tracks from different bunch crossings (out-of-time pile-up).

The BBC is an array of plastic scintillator detectors designed to detect high$-\eta$ particles produced in the forward direction. The BBC consists of two identical detectors placed at ± 3.74 m from the IP. Each detector is formed by 36 hexagonal scintillator tiles, covering a pseudorapidity range of $2.1 < |\eta| < 3.3$, and 18 large tiles covering $3.3 < |\eta| < 5.0$, respectively. For the CEP events, it is used as a rapidity gap veto, to ensure the rapidity gaps between the central produced system and forward-scattered protons.

The ZDC's main function is to measure particles produced in the forward direction (at a near zero degree angle). They are placed on each side of the IP at a distance of 18 m, directly in line with the STAR beam pipe behind the DX dipole magnets. These magnets deflect charged particles, including the forward protons. They are used to detect beam energy neutrons produced in the forward direction close to the beam direction. Both BBC and ZDC are used to ensure rapidity gap within their acceptance, hence reducing background due to the non-exclusive events at the trigger level.

The RPs are used to detect and measure forward protons scattered at very small angles (few mrad), whose trajectories are contained in the accelerator beam pipe. For that purpose, the STAR experiment was upgraded with the RP system previously used by the PP2PP experiment [22]. Two RP stations were installed on each side of the IP at a distance of of 15.8 m and 17.6 m from the IP. The location of the RPs, top and side views, and the coordinate system are shown schematically in Figure 3. Each RP station has two movable RP vessels: one above and one below the beam pipe. Each stainless steel RP vessel houses a Silicon Strip Detector (SSD) package and a scintillation counter. The SSD package consists of four SSDs measuring proton position in the $x - y$ plane, two measuring $x-$coordinate

and two measuring $y-$coordinate. The detector package has transverse size 5×8 cm^2 and a depth 3.5 cm. The silicon sensor is 400 μm thick, while the trigger scintillator is 5 mm thick. The strips in the silicon detectors are ≈ 100 μm wide. The typical distance of the first horizontal strip from the beam was about 2 cm. Having two RP stations on each side allows momentum reconstruction of scattered protons. The scintillation counter was used to trigger on forward protons. Each trigger counter was read out by two photomultipliers. The stainless steel vessel separates the detector package from the machine vacuum allowing operation of the package at normal atmospheric pressure.
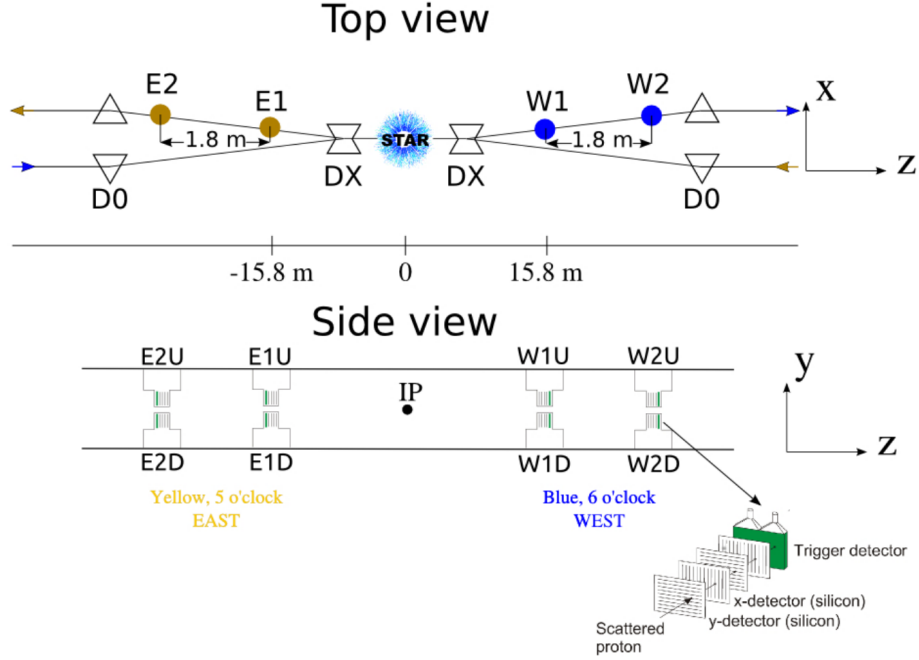

Figure 3. The layout of the RP setup at STAR (not to scale) for measuring forward protons. Top (x, z) and side (y, z) views are shown. Two sets of RPs, labeled (W1, W2) and (E1, E2) were installed between the DX and D0 magnets, at 15.8 m and 17.6 m, on either side of the IP. The detector package has transverse size 5×8 cm^2 and a depth 3.5 cm. The silicon sensor is 400 μm thick, while the trigger scintillator is 5 mm thick. The strips in the silicon detectors are ≈ 100 μm wide. Two dipole magnets, DX and D0, which bend the beams into and out of the IP, are also shown. Top view with highlighted Roman Pot stations E1, E2, W1, W2 and dipole magnets DX, D0. Side view with depicted Roman Pots. Taken from Ref. [23].

There is an RP naming convention that denotes the position of each RP. The RP names are in the following format: side of the IP (E or W), station (1 or 2), and orientation (U or D). For example, the first RP, as measured away from the IP, located on the west side of the IP above the beam line, is called W1U. Moreover, the RP system is divided into four branches (EU, ED, WU, and WD), in which proton tracks can be reconstructed. A branch is composed of two RP on the same side of the IP (E or W) and with the same orientation (U or D). For example, the EU branch is composed of E1U and E2U RPs.

The RP stations are placed behind the DX magnet, the RHIC-lattice dipole magnet closest to the IP. This positioning allows the measurement of the momentum vector of the

scattered protons at the detection point. The symmetry of the RHIC rings requires that the magnetic fields in the DX magnets are the same, the relative differences of DX magnet strengths are at the 10^{-3} level [24]. The RP layout ensures that no special beam conditions were needed to operate the RP detectors.

After the RP installation, a survey was performed to determine the position in space of the first strip in each detector package in the STAR coordinate system, the so-called baseline survey alignment. Corrections to the baseline survey alignment were obtained using elastically scattered protons. The collinearity constraint was applied, which required that the two reconstructed tracks on each side of the IP lie on the same straight line. The alignment method is the same as described in Ref. [23] and used in Ref. [3, 23, 24]. The obtained corrections are applied to correct the position of reconstructed points. The average final correction over all runs is 20 ± 10 μm is consistent with the one obtained in Ref. [24].

3   Triggers

The trigger for CEP events was based on the topology of those events. The following trigger conditions were required:

1. At least one proton on each side of IP. A signal, an energy deposit consistent with a minimum ionizing particle (MIP) in time with the beam crossing, was required in exactly one branch on each side of the IP. A veto was imposed on the other branches to reject either proton dissociation or pile-up events. The signal ensures presence of at least two forward-scattered protons.

2. Two charged particles in central rapidity. This was implemented by requiring the TOF multiplicity ≥ 2. The upper limit on the TOF multiplicity (≤ 10) was applied to reject high multiplicity events. This allowed good acceptance for four-pion events and avoided rejection of CEP events which could overlap with a small level of noise.

3. A rapidity gap between the central system and forward protons. A veto on signal consistent with minimum ionizing particle in small or large BBC tiles, or energy deposit in the ZDCs above a few tens of GeV on either side of the IP was used to ensure the double-gap topology typical of CEP events.

4   Event Selection

Three primary sets of selection criteria are implemented to select CEP events: 1) selection of forward protons; 2) selection of tracks in the TPC: particle identification associated with the tracks and fiducial acceptance of the tracks in the TPC; 3) exclusivity cut using balance of transverse momentum (p_T) of all measured particles, (p_T^{miss}). The cuts are chosen to ensure high signal to noise ratio and efficiency. They are explained in more detail in the following sections.

4.1 RP tracks

In order to reconstruct the position and momentum of the forward protons, we follow the approach from Ref. [3, 23, 24]. First, space points are reconstructed in each RP. Second, events with only one space point per RP are used to reconstruct a track. For these events, the transverse momentum of the protons (p_x, p_y) is reconstructed based on the positions of space points assuming a constant and uniform magnetic field inside the DX magnet.

To select CEP event candidates, exactly one RP track on each side of the IP is required. Each track must have at least three out of four SSD planes used in its space point reconstruction in each RP. Furthermore, to ensure high acceptance, RP efficiency, and low systematic uncertainties, the reconstructed protons have to have momenta (p_x, p_y) inside a fiducial volume, defined in Equation 4.1 and shown in Figure 4.
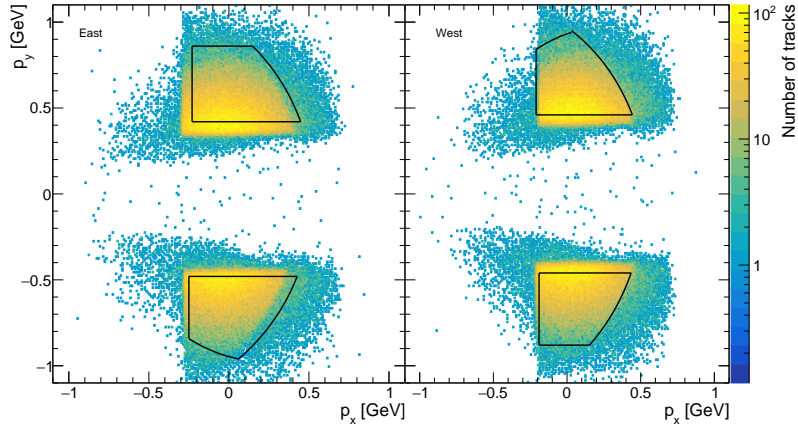

Figure 4. The RP fiducial volume shown with black solid lines on top of the combined distributions of forward protons' momenta p_y vs. p_x reconstructed with the East and West RP stations.

$$|p_y| > p_y^{\min} \wedge p_x > p_x^{\min}$$
$$(p_x + p_x^{\text{center}})^2 + p_y^2 < R^2$$
$$(p_y > 0 \quad \text{for EU and WU}) \wedge (p_y < 0 \quad \text{for ED and WD}) \tag{4.1}$$
$$|p_y| < p_y^{\max} \quad \text{for EU and WD}$$
$$(p_x + \bar{p}_x^{\text{center}})^2 + p_y^2 < \bar{R}^2 \quad \text{for ED and WU,}$$

where the parameters are summarized in Table 1.

Most of the scattered protons are at low $|p_y|$, since the cross section drops with increasing scattering angle (i.e. increasing $|p_y|$). At the same time, the probability of measuring a proton from the beam halo[2] also increases as the RPs get closer to the beam axis (decreasing $|p_y|$). In order to maximize the acceptance, it is necessary to get $|p_y|$ as low as possible for each branch separately. Hence, the chosen fiducial volume allows high acceptance and high signal to noise ratio at the same time.

---

[2]The beam halo consists of particles traveling with the main beam, most of which are protons. These particles are typically located at transverse distances greater than 10σ of the beam size from the beam center.

	EU	ED	WU	WD
$p_x^{\min}$ (GeV)	-0.23	-0.25	-0.21	-0.19
$p_y^{\min}$ (GeV)	0.42	0.48	0.46	0.46
$p_y^{\max}$ (GeV)	0.86	0.84	0.84	0.88
p_x^{center} (GeV)	0.64	0.7	0.6	0.7
R^2 (GeV^2)	1.36	1.5	1.3	1.5
$\bar{p}_x^{\text{center}}$ (GeV)	0.0	-0.25	-0.28	0.0
$p_x^{\max}$ (GeV)	0.0	0.06	0.03	0.0
$\bar{R}^2$ (GeV^2)	0.0	0.959	0.946	0.0

Table 1. The summary of parameters defining the fiducial volume.

4.2 Primary vertex and its z-position

In order to reject events with more than one inelastic interaction per bunch crossing, exactly one primary vertex is required in each event. In addition, the vertex must be reconstructed within ±100 cm from the IP along the $z-$axis to assure high event acceptance.

4.3 TPC tracks

In order to select tracks in time with the bunch crossing and to extend the momentum range in PID of the central state, only tracks matching valid TOF hits are used. Therefore, tracks are required to have $p_\mathsf{T} > 250$ MeV that is above strongly raising acceptance of TPC. This also makes it sufficient to reach the TOF detector. Also, quality track criteria are imposed to achieve good momentum and energy loss resolution. Namely, a minimum of 20 hits in the TPC are used for the track reconstruction ($N_{\text{hits}}^{\text{fit}} \geq 20$) out of which a minimum of 15 hits to calculate $\langle dE/dx \rangle$ ($N_{\text{hits}}^{\langle dE/dx \rangle} \geq 15$). In addition to the above, only tracks with a good match to the primary vertex are further analyzed. A track has a good match to a vertex if its distance of closest approach (DCA) to the vertex in the transverse plane (DCA$_{xy}$) is smaller than 1.5 cm and in the $z-$direction (DCA$_z$) is smaller than 1.0 cm.

To select CEP event candidates, only events with exactly two tracks satisfying the above criteria and with opposite charge are considered. To ensure high geometric acceptance and efficiency, the tracks are further required to have pseudorapidity within the fiducial acceptance defined by Equation 4.2:

$$(-\frac{1}{250}z_{\text{vtx}} - 0.9 < \eta < -\frac{1}{250}z_{\text{vtx}} + 0.9) \wedge (|\eta| < 0.9), \qquad (4.2)$$

where η is the track's pseudorapidity and z_{vtx} is the $z-$position of the primary vertex in centimeters. The equation takes into account the change of the acceptance in pseudorapidity as a function of the $z-$position of the primary vertex.

4.4 Exclusivity cut

Finally, an exclusivity requirement is imposed to select CEP event candidates. The detection and reconstruction of forward-scattered protons in the RP detectors, together with

the central system, allow the calculation of the missing transverse momentum, defined as the sum of the transverse momenta of all measured particles:

$$p_T^{\mathrm{miss}} := |\,(\vec{p}_p + \vec{p}_{h^+} + \vec{p}_{h^-} + \vec{p}_p)_T\,|. \tag{4.3}$$

In the CEP processes, the p_T^{miss} should be equal to zero due to momentum conservation. The distribution of p_T^{miss} of the events passing the first two set of criteria is shown in Figure 5. The peak at low p_T^{miss} is due to the exclusive events. In each coordinate in the $(p_x^{\mathrm{miss}}, p_y^{\mathrm{miss}})$ space, the peaks are centered at zero. However, in any event the $(p_x^{\mathrm{miss}}, p_y^{\mathrm{miss}})$ does not have to be zero at the same time, hence the peak in the p_T^{miss} is shifted. Its width is mostly due to the beam angular divergence of 90 μrad. Events are selected if they have $p_T^{\mathrm{miss}} < 120$ MeV as illustrated by the black dashedline in Figure 5. The non-exclusive background is estimated by projecting a fitted second-degree polynomial outside of the cut, $160 < p_T^{\mathrm{miss}} < 300$ MeV, with the constant term set to zero. The red line is the fit and its projection into the signal region.

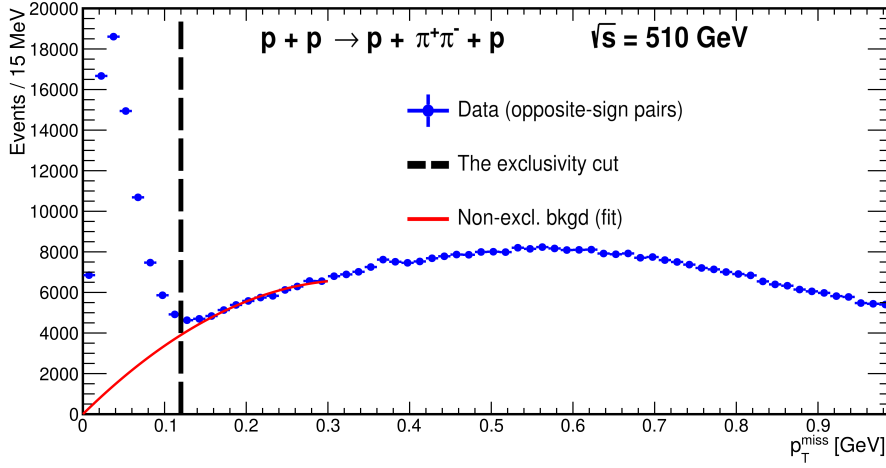**Figure 5**. The distribution p_T^{miss} for $\pi^+\pi^-$ CEP event candidates with the p_T^{miss} cut illustrated by the black dashed line. The non-exclusive background is fitted using a second-degree polynomial with the constant term set to zero. The fit is depicted by the red line and projected into the signal region.

4.5 Particle identification

The PID is based on $\langle dE/dx \rangle$ information from the TPC and time of hit from the TOF detector. The PID is based on combined information from the TPC, particle's $\langle dE/dx \rangle$, and its time of hit in the TOF detector. The combined information is used to identify hadron pairs: $\pi^+\pi^-, K^+K^-$, or $p\bar{p}$. For this purpose, the χ^2 of the pair hypothesis is defined as:

$$\chi^2_{\langle dE/dx \rangle}(h^+h^-) = (n\sigma_{h^+})^2 + (n\sigma_{h^-})^2 , \tag{4.4}$$

where $n\sigma_h$ is the number of standard deviations between the measured and the expected energy loss [25] for a given hadron. Figure 6 (left) shows log of the $\langle dE/dx \rangle$ of charged

particles as a function of log of their momentum. Pions, kaons, and protons are clearly seen.
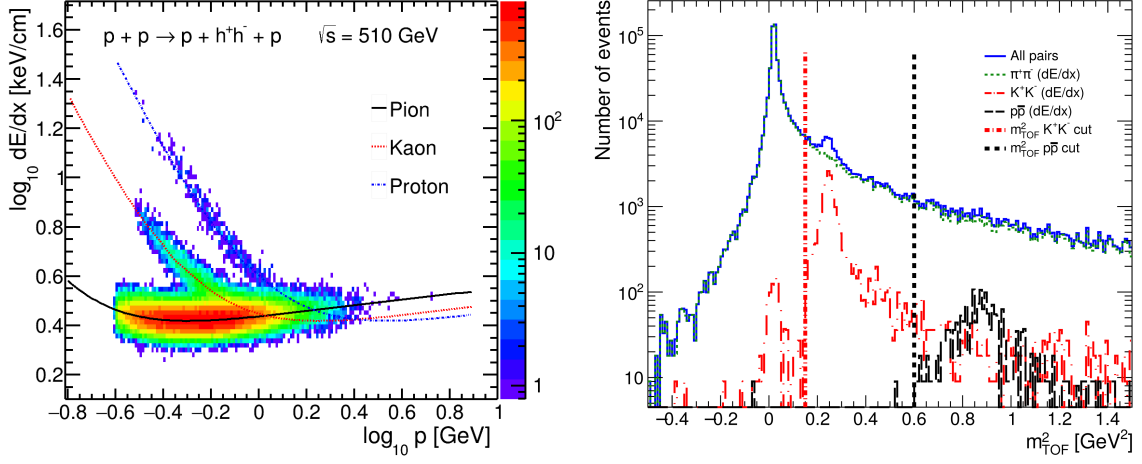

Figure 6. Left: the energy loss $\langle dE/dx \rangle$ of central charged particles as a function of their momenta for CEP event candidates. Colored curves illustrate expected values for pions, kaons, and protons. Right: distributions of invariant mass squared m^2_{TOF} of pions, kaons, and protons. Particle type is identified solely based on $\langle dE/dx \rangle$ information. Applied PID cuts are highlighted by dot-dashed lines.

To extend the PID capabilities of $\langle dE/dx \rangle$ method, the TOF information is used. However, the standard method based on the inverse particle velocity $(1/\beta)$ cannot be used for CEP events. This is due to lack of the starting time of the collision, which is reconstructed from a signal in VPD detectors. Instead, the difference in particle time of flight can be used for identifying particle pairs without an explicitly measured starting time. The method assumes that both tracks originate from the same vertex and have the same mass. Then, squared mass of particle, m^2_{TOF}, can be derived from the measured TOF time difference between particles:

$$t_2 - t_1 = L_2 \sqrt{1 + \frac{m^2_{\mathrm{TOF}}}{p_2^2}} - L_1 \sqrt{1 + \frac{m^2_{\mathrm{TOF}}}{p_1^2}}, \qquad (4.5)$$

where $t_{1,2}$ are time of the tracks' detection in TOF. $L_{1,2}$ and $p_{1,2}$ denote the track lengths and momenta of the particles, respectively, as determined from their trajectories measured by the TPC.

The m^2_{TOF} distributions of pions, kaons, and protons, identified solely based on $\langle dE/dx \rangle$ information, can be seen in Figure 6 (right). Although peaks close to each particles' invariant mass squared values are seen.Due to the resolution effects, negative, nonphysical values can be seen.

Particle pairs are identified based on the following hypothesis. First, the $p\bar{p}$ pair hypothesis is checked:

$$(\chi^2_{\langle dE/dx \rangle}(p\bar{p}) < 9) \wedge (m^2_{\mathrm{TOF}} > 0.6 \ \mathrm{GeV}^2) \wedge (\chi^2_{\langle dE/dx \rangle}(K^+K^-) > 9) \wedge (\chi^2_{\langle dE/dx \rangle}(\pi^+\pi^-) > 9).$$

$$(4.6)$$

If the hypothesis is satisfied the pair is identified as $p\bar{p}$ pair, if not the K^+K^- pair hypothesis is verified:

$$(\chi^2_{\langle dE/dx\rangle}(K^+K^-) < 9) \wedge (m^2_{\text{TOF}} > 0.15 \text{ GeV}^2) \wedge (\chi^2_{\langle dE/dx\rangle}(p\bar{p}) > 9) \wedge (\chi^2_{\langle dE/dx\rangle}(\pi^+\pi^-) > 9). \tag{4.7}$$

If neither of $p\bar{p}$ nor K^+K^- pair hypothesis is satisfied, the $\pi^+\pi^-$ pair is assumed and the $\pi^+\pi^-$ pair hypothesis is checked:

$$\chi^2_{\langle dE/dx\rangle}(\pi^+\pi^-) < 12. \tag{4.8}$$

This PID technique is designed to minimize misidentification of $\pi^+\pi^-$ pairs as K^+K^- or $p\bar{p}$ pairs. In addition, the PID is restricted to fiducial acceptance with high track reconstruction efficiency and high pair identification efficiency. The misidentified pairs form a negligible exclusive background ($< 1\%$), as discussed in section 5. In summary, the fiducial acceptance of the central hadronic state is defined as:

$$p_{\mathsf{T}}(\pi) > 0.25 \text{ GeV}, \tag{4.9}$$

$$(p_{\mathsf{T}}(K) > 0.3 \text{ GeV}) \wedge (min(p_{\mathsf{T}}(K^+), p_{\mathsf{T}}(K^-)) < 0.7 \text{ GeV}), \tag{4.10}$$

$$(p_{\mathsf{T}}(p) > 0.4 \text{ GeV}) \wedge (min(p_{\mathsf{T}}(p), p_{\mathsf{T}}(\bar{p})) < 1.1 \text{ GeV}). \tag{4.11}$$

After all the above selection cuts, there are 86008 $\pi^+\pi^-$, 2454 K^+K^-, and 225 $p\bar{p}$ CEP events.

5 Background estimation

In this section, sources of backgrounds and their quantitative determination are discussed. There are two main sources of background: an exclusive and a non-exclusive background.

The exclusive background comes comes primarily from incorrectly identified particles species. Namely, when the event passes all the selection criteria but is miss-identified due to the incorrectly identified particle species. The phase space of the measurement is limited to preserve high pair identification efficiency and low probability of miss-identification. This background is estimated to be $< 1\%$ therefore negligible.

The non-exclusive background is the dominant source of background. It arises from non-exclusive events that imitate the topology of CEP of h^+h^-: two forward protons, two opposite sign central tracks and large rapidity gaps. The most common sources of the non-exclusive background are:

1. **Accidental coincidences (pile-up):** there can be accidental coincidences of the forward and central system. Like, for example, the overlap of elastic scattering with another inelastic interaction in the central system can imitate a CEP event. Or, it can also be an overlap of a single diffraction event with a proton from the beam halo.

2. **Central Diffraction:** like a CEP event with a higher number of produced particles, where only two are detected.

₃₂₆ **The non-exclusive background subtraction** is carried out using missing transverse
₃₂₇ momentum, Equation 4.3. The following method is described for the invariant mass of
₃₂₈ $\pi^+\pi^-$ ($m(\pi^+\pi^-)$), but works for other observables used here.

1. The amount of non-exclusive background sample is estimated in two steps. First, the
   $p_\mathsf{T}^{\mathrm{miss}}$ distribution (see Figure 5) is fitted with a second-degree polynomial with the
   constant term fixed to zero in the sideband. Second, the fit is extrapolated into the
   signal region to obtain the amount of background.

2. The correlation between $m(\pi^+\pi^-)$ and $p_\mathsf{T}^{\mathrm{miss}}$ is plotted with the same binning as the
   $m(\pi^+\pi^-)$ distribution.

3. The $p_\mathsf{T}^{\mathrm{miss}}$ is projected onto $m(\pi^+\pi^-)$ in the range from 160 to 220 MeV. The range
   is selected to be as close as possible to the signal region and at the same time out of
   the signal region. There is an assumption that the shape of the background in the
   selected range is the same as in the signal region.

4. The obtained background distribution is normalized to the expected background
   amount determined in the first step.

5. Finally, the normalized background distribution is subtracted separately from the
   $m(\pi^+\pi^-)$ distribution for each bin of the distribution.

₃₄₃ Using this method, the amount of non-exclusive background is found to be $19.4 \pm 0.4\%$
₃₄₄ for $\pi^+\pi^-$ pairs, $12.1 \pm 0.8\%$ for K^+K^- pairs, and $43 \pm 5\%$ for $p\bar{p}$ pairs.

6 Corrections

₃₄₆ The differential fiducial cross section in every bin of measured quantity of interest, q, is
₃₄₇ obtained using the formula Equation 6.1:

$$\frac{d\sigma}{dq}(q) = \frac{1}{\Delta q} \times \frac{N^{\mathrm{w}}(q) - N_{\mathrm{bkgd}}^{\mathrm{w}}(q)}{L_{\mathrm{int}}^{\mathrm{eff}}}, \tag{6.1}$$

₃₄₉ where $N^{\mathrm{w}}(q)$ and $N_{\mathrm{bkgd}}^{\mathrm{w}}(q)$ are the weighted numbers of observed and background events
₃₅₀ in the given bin, where the weight is the inverse total efficiency calculated as the product
₃₅₁ of all efficiencies for the given event. Δq is the width of the bin, and $L_{\mathrm{int}}^{\mathrm{eff}}$ is the effective
₃₅₂ integrated luminosity defined as:

$$L_{\mathrm{int}}^{\mathrm{eff}} = \sum_{\mathrm{run}} L_{\mathrm{int}}^{\mathrm{run}} \times P_{\mathrm{retain}}^{\mathrm{CEP}}(L_{\mathrm{inst}}^{\mathrm{run}}), \tag{6.2}$$

₃₅₄ where $L_{\mathrm{int}}^{\mathrm{run}}$ is the integrated luminosity for the given run and $P_{\mathrm{retain}}^{\mathrm{CEP}}(L_{\mathrm{int}}^{\mathrm{run}})$ is the probability
₃₅₅ of retaining the CEP event as a function of the instantaneous luminosity ($L_{\mathrm{inst}}^{\mathrm{run}}$).
₃₅₆ The integrated luminosity is 121 ± 6 pb^{-1}. It has to be corrected to account for
₃₅₇ the probability of retaining CEP events, which depends on the instantaneous luminosity.
₃₅₈ There is a high probability that an exclusive event overlaps with another process and

is therefore rejected. This occurs because the CEP trigger includes vetoes ensuring the characteristic double-gap rapidity topology of CEP events. The probability of retaining CEP events is calculated using zero-bias data, taking into account both online and offline vetoes. The online vetoes were part of the trigger definition as described in section 3. The offline veto comes from the requirement of one reconstructed primary TOF vertex. The probability is studied separately for each run[3] and is fitted with an exponential function of the instantaneous luminosity. This reflects the expected Poisson-like behavior of the probability that no interaction occurs in a bunch crossing. The probability of retaining the CEP event is found to be independent of the choice of the RP branch combination. The values of $P_{\mathrm{retain}}^{\mathrm{CEP}}(L_{\mathrm{inst}}^{\mathrm{run}})$ vary between $15 - 40\%$, which leads to the effective integrated luminosity of $L_{\mathrm{int}}^{\mathrm{eff}} = 25.6 \pm 1.6$ pb^{-1}.

To determine the TPC and TOF detector efficiencies, an embedding technique is used to simulate the data taking environment. First, MC generated particles are processed using a GEANT3 [26] detector simulation implementing STAR geometry. Second, the output, which mimics raw data from collisions, is mixed with zero-bias data representing an underlying event.

The TPC track acceptance, reconstruction, and selection efficiencies are studied together and they are used as a TPC efficiency. This efficiency is calculated by tracking how many MC particles are properly reconstructed from the embedded sample. The corrections are calculated as function of $(p_{\mathsf{T}}, \eta, z_{\mathrm{vtx}})$. The typical TPC efficiencies are 83% for $\pi^{\pm}$, 63% for $K^{\pm}$, and 78% for p and $\overline{p}$. The typical statistical uncertainties on those values are $< 1\%$. The efficiencies for kaons are lower due to weak decays of kaons in front of or inside the TPC.

The TOF acceptance, hit reconstruction and TPC track matching to a TOF hit efficiencies are studied together as a TOF efficiency. The efficiency is determined from embedding and compared with data-driven tag-and-probe method based on decays of K_S^0 to $\pi^+\pi^-$. The tagged particle is measured by the TPC and the TOF detectors, whereas the probed particle is measured by the TPC and is under study in the TOF. The TOF efficiency for the probed track $\epsilon_{\mathrm{TOF}}^{\mathrm{probe}}$ is calculated as the ratio of two different yields of $\pi^+\pi^-$ pairs satisfying criteria for K_S^0 candidates:

$$\epsilon_{\mathrm{TOF}}^{\mathrm{probe}} = \frac{N_{\mathrm{TOF}}^{\mathrm{both}}}{N_{\mathrm{TOF}}^{\mathrm{tag}}}, \tag{6.3}$$

where $N_{\mathrm{TOF}}^{\mathrm{both}}$ and $N_{\mathrm{TOF}}^{\mathrm{tag}}$ are the yields of K_S^0 candidates where both pion tracks have TOF hits and where only the tagged pion track is matched to the TOF, respectively. The typical TOF efficiencies are 63% for $\pi^{\pm}$, 60% for $K^{\pm}$, and 59% for p and $\overline{p}$.

The criterion on the TPC z-vertex position, discussed in subsection 4.2, reduces the accepted luminosity relative to the luminosity delivered by the collider. In order to account for this loss, z-positions of primary vertices for each RHIC fill are independently fitted by a normal distribution. Then, the efficiency is estimated based on the obtained values of the

---

[3]A run at STAR refers to a dataset collected during a specific time interval when data was recorded; this typically between 30 minutes to 2 hours.

mean and standard deviation. Another method is also used. It calculates the fraction of lost luminosity directly from the z_{vtx} distribution. The difference between the two methods is about 2% and is independent of the fill number. Therefore, the average of the two efficiency corrections is used to correct the data. A typical vertex-cut efficiency is 90%.

The PID efficiency is defined as the probability that the hadron (h^+h^-) pair passes the corresponding pair selection criteria discussed in subsection 4.5. The same embedded samples that are used for TPC and TOF detector efficiencies are used to determine the PID efficiencies. These are studied as a function of the maximum and minimum true transverse momenta of particles in the pair ($p_{\text{T}}^{\text{max}}, p_{\text{T}}^{\text{min}}$). The efficiency is applied as a function of the ($p_{\text{T}}^{\text{max}}, p_{\text{T}}^{\text{min}}$). The average PID efficiency for $\pi^+\pi^-$ pairs is higher than 99%. At higher values of $p_{\text{T}}^{\text{min}}$, the efficiencies for K^+K^- and $p\bar{p}$ drop significantly due to the requirement of $\chi^2_{\langle dE/dx \rangle}(\pi^+\pi^-) > 9$, which is used to limit misidentification of $\pi^+\pi^-$ pairs in the K^+K^- and $p\bar{p}$ samples. The typical efficiencies for K^+K^- and $p\bar{p}$ pairs are 93% and 95%, repsecively.

The TPC vertex efficiency is studied using global tracks, which are tracks that are not associated with the primary vertex. Events that mimic CEP are examined to determine if they form a good primary vertex. These events are required to have exactly two good-quality, global TPC tracks matched with TOF. The same good-quality track criteria as described in subsection 4.3 are applied. The efficiency is determined as follows:

$$\epsilon_{\text{vertex}} = \frac{N_{\text{vertices}}^{\text{reco}}}{N_{\text{vertices}}^{\text{examined}}}, \tag{6.4}$$

where $N_{\text{vertices}}^{\text{reco}}$ and $N_{\text{vertices}}^{\text{examined}}$ are the number of successfully reconstructed and examined vertices, respectively. The average TPC vertex reconstruction efficiency is 89.6%.

A small fraction of CEP events is lost due to the exclusivity criterion, $p_{\text{T}}^{\text{miss}} < 120$ MeV. The efficiency of the exclusivity criterion is determined as the relative amount of CEP events below the exclusivity criterion from data and MC samples. An MC technique is used to describe the $p_{\text{T}}^{\text{miss}}$ distribution. The MC sample is generated in p_x^{miss} and p_y^{miss} missing space based on the parameters of the fits on p_x^{miss} and p_y^{miss} from the data. The average efficiency from the data and MC is used with typical value above 99%.

In order to calculate the RP acceptance and track reconstruction and selection efficiency, a dedicated tool (*ppSim*) based on GEANT4 [27] is developed to simulate response of the RP detectors, as described in Ref. [23, 24]. It includes full implementation of the beamline elements. It also accounts for the background contribution from scattered protons interacting with the material in front of RPs, and inoperable SVX readout chips [24]. In order to fully reproduce the collision environment, a single proton is generated with total energy of 254.9 GeV. The proton momentum is smeared by the beam angular divergence and propagated through the beamline to the RPs. The *ppSim* output is embedded in the zero-bias events.

There are two parts to the RP efficiency: the detector efficiency and the proton selection efficiency. The detector efficiency for a given branch describes the probability that a proton is measured and reconstructed in that branch. It is calculated as the probability that a single good-quality RP track is reconstructed in the branch. This track must be

matched with a true-level primary forward proton. The typical RP detector efficiency is about 98%. That efficiency is compared with a data-driven method, which is based on reconstruction of elastic events. The efficiencies agree within 2σ of statistical uncertainties. The proton selection efficiency reflects the probability that the reconstructed proton will be selected by the reconstruction algorithm. Any additional background from pile-up or noise will lower the proton selection efficiency. The typical value of the RP efficiency for a given branch is about 88%.

Efficiencies quoted above have statistical uncertainties at a fraction of a percent level. Hence, they are negligible compared to the statistical uncertainties of the results. Therefore, they are neither quoted nor propagated.

7 Systematic Uncertainties

In this section, we describe how systematic uncertainties are obtained. We find that only the background subtraction systematic uncertainty is bin dependent. All other systematic uncertainties are not bin dependent. The following systematic uncertainties are evaluated for each presented distribution separately:

1. **Background subtraction:** the systematic uncertainty related to the non-exclusive background subtraction discussed in section 5. It is studied by varying the range of the projection: from 170 to 210 MeV (smaller range) and from 140 to 250 MeV (wider range). The subtraction is performed for the ranges described previously. The obtained fiducial differential cross sections for CEP of h^+h^- pairs as a function $m(h^+h^-)$ are compared with the nominal one. The uncertainty is taken as the average of absolute deviations for each bin separately. There is another source of the systematic uncertainty, which is due to the statistical uncertainty of the size of the non-exclusive background sample. This uncertainty is common for all the bins. The weighted mean of uncertainties of the background subtraction in the invariant mass distribution of $\pi^+\pi^-$, K^+K^-, and $p\bar{p}$ pairs are 0.4%, 0.8%, and 3.3%, respectively. Only this systematic uncertainty is bin dependent.

2. **RP efficiency correction:** the systematic uncertainty associated with the RP efficiency corrections for a single proton is studied from run-by-run variations in each RP branch separately. An average variation is approximately 1.5% for a single proton resulting in the total RP systematic uncertainty on the fiducial differential cross sections to be 2.4%.

3. **TPC efficiency correction:** the uncertainty is studied by varying the TPC track selection criteria ($N_{\text{hits}}^{\text{fit}}$ and $N_{\text{hits}}^{\langle dE/dx \rangle}$) and applying the TPC efficiency corrections corresponding to the given set of selection criteria. The obtained fiducial differential cross sections are compared with the cross section calculated with corrections as described in section 6. The typical uncertainties on the fiducial differential cross sections are $^{+7}_{-4}$%, $^{+7}_{-4}$%, and $^{+4}_{-4}$% for $\pi^+\pi^-$, K^+K^-, and $p\bar{p}$ pairs, respectively.

4. **TOF efficiency correction:** the uncertainty is studied by comparing the corrections obtained from the embedding and the data-driven tag-and-probe method based on $K_S^0 \to \pi^+\pi^-$ decays. The difference between the embedding and the tag-and-probe method is found to be about 1.0% per a single track. In addition, the corrections from the embedding are calculated as function of (p_T, η, z_{vtx}) with different binning applied. The obtained fiducial differential cross sections are compared with the cross section calculated with corrections as described in section 6. This method of applying the TOF matching efficiency corrections leads to an addition uncertainty. The typical total TOF uncertainty on the fiducial differential cross sections is $^{+1}_{-2}\%$ for $\pi^+\pi^-$, K^+K^-, and $p\bar{p}$ pairs.

5. **TPC vertex reconstruction:** the systematic uncertainty is determined by varying the good primary vertex criteria (DCA_{xy} and DCA_z) and applying the TPC vertex reconstruction efficiency corrections corresponding to the given set of vertex criteria. The uncertainty on the fiducial differential cross section is $^{+2.6}_{-1.0}\%$.

6. **TPC z-vertex criterion:** the uncertainty is calculated as half of the difference between the two methods used. The systematic uncertainty is determined to be independent of the fill and is 1.1%.

7. **Exclusivity p_T^{miss} cut:** the systematic uncertainty is 0.4% as the difference between efficiencies obtained from MC and data samples.

8. **Particle identification:** the uncertainty is studied by varying the pair identification criteria. The typical change of $< 1\%$, $^{+4}_{-5}\%$ and $^{+4}_{-5}\%$ in the fiducial differential cross section is observed for $\pi^+\pi^-$, K^+K^-, and $p\bar{p}$ pairs, respectively. This change results from applying looser and tighter identification criteria and correcting for the corresponding PID efficiency. The looser condition uses the $\chi^2_{\langle dE/dx \rangle}(h^+h^-) < 12$ condition instead of $\chi^2_{\langle dE/dx \rangle}(h^+h^-) < 9$ in Equation 4.8 and in Equation 4.7. The values for the cuts m_{TOF}^2 are 0.1 and 0.55 GeV^2 for the kaon and proton hypotheses, respectively. The pion hypothesis Equation 4.6 is changed to $\chi^2_{\langle dE/dx \rangle}(\pi^+\pi^-) < 15$. The tighter cut uses the $\chi^2_{\langle dE/dx \rangle}(h^+h^-) < 7$ condition instead of $\chi^2_{\langle dE/dx \rangle}(h^+h^-) < 9$ in Equation 4.8 and in Equation 4.7. The values for the cuts m_{TOF}^2 are 0.2 and 0.7 GeV^2 for the kaon and proton hypotheses, respectively. The pion hypothesis Equation 4.6 is changed to $\chi^2_{\langle dE/dx \rangle}(\pi^+\pi^-) < 9$.

9. **The luminosity uncertainty**. There are two parts of the luminosity uncertainty: luminosity calibration based on van der Meer scans [28] and the probability of retaining a CEP event, dependent on instantaneous luminosity. The first, contributes to the integrated luminosity uncertainty and is 5% [29]. The second, is evaluated to be 4%. Thus, the total uncertainty on effective integrated luminosity Equation 6.2 is 6.4%. This systematic vertical scale uncertainty is not plotted on the results.

Systematic uncertainties for the integrated fiducial cross sections for CEP of $\pi^+\pi^-$, K^+K^-, and $p\bar{p}$ pairs are shown in Table 2.

	$\delta_{\mathrm{syst}}/\sigma_{\mathrm{fid}}$ [%]				
Particle species	TPC	TOF	RP	Other	Total
$\pi^+\pi^-$	$^{+7}_{-4}$	$^{+1}_{-2}$	2.4	$^{+3}_{-2}$	$^{+8}_{-5}$
K^+K^-	$^{+7}_{-4}$	$^{+1}_{-2}$	2.4	$^{+5}_{-4}$	$^{+9}_{-7}$
$p\bar{p}$	$^{+4}_{-4}$	$^{+1}_{-2}$	2.4	$^{+5}_{-4}$	$^{+7}_{-6}$

Table 2. Typical systematic uncertainties for the integrated fiducial cross section for CEP of $\pi^+\pi^-$, K^+K^-, and $p\bar{p}$ pairs. The numbers represent the relative systematic uncertainty of the integrated fiducial cross section in percentage.

8   Results

In this section, the results on differential fiducial cross sections and the integrated fiducial cross sections are presented. The fiducial volume of the measurement is common for all the presented results and it is defined in Equation 4.1 for the protons in the RPs, and depending the specific central hadronic state in Equation 4.2, and Equations 4.9−4.11.

8.1   Differential fiducial cross sections

In this section, differential fiducial cross sections are presented and compared with predictions from GRANIITTI [30]. GRANIITTI is an MC event generator designed for high energy diffraction with focus on the CEP. It combines up-to-date phenomenological models and approaches [6, 7, 31]. GRANIITTI is the only model that includes a full parametric resonant spectrum, continuum production with significant interference effects between them. In this analysis, the newest version of GRANIITTI v. 1.090 is used, which was tuned to the latest STAR CEP results at $\sqrt{s} = 200$ GeV [3, 32].

Figure 7 shows the differential fiducial cross sections for CEP of $\pi^+\pi^-$, K^+K^-, and $p\bar{p}$ pairs as a function of the difference between azimuthal angles of the forward protons $\Delta\varphi$. Strong suppression close to $\Delta\varphi = 90°$ is due to the limited azimuthal acceptance in RP detector system. The acceptance naturally divides the phase space into two ranges of $\Delta\varphi$, where different IPomeron dynamics and absorption effects are expected. Therefore, GRANIITTI predictions were produced separately for each $\Delta\varphi$ region: $\Delta\varphi > 90°$ and $\Delta\varphi < 90°$.

GRANIITTI predictions are calculated including both continuum (Cont.) and resonance (Res.) contributions. The resonances used in the model are summarized in Table 3. Subsequently, the predictions are scaled to match the integrated cross section in each $\Delta\varphi$ region. If the scaling is within 10% no scaling is applied. Moreover, the pure continuum is shown without scaling applied for $\pi^+\pi^-$ and K^+K^- pairs and with scaling for $p\bar{p}$ pairs. The hadron pairs are smeared based on the p_{T} resolution and the same fiducial criteria on forward protons and central hadron as described in section 4 are applied.

Figure 8 shows differential fiducial cross sections of $\pi^+\pi^-$, K^+K^-, and $p\bar{p}$ pairs as a function of the invariant mass of the pair in two $\Delta\varphi$ regions measured within the STAR acceptance in proton-proton collisions at $\sqrt{s} = 510$ GeV. GRANIITTI predictions are shown as well.
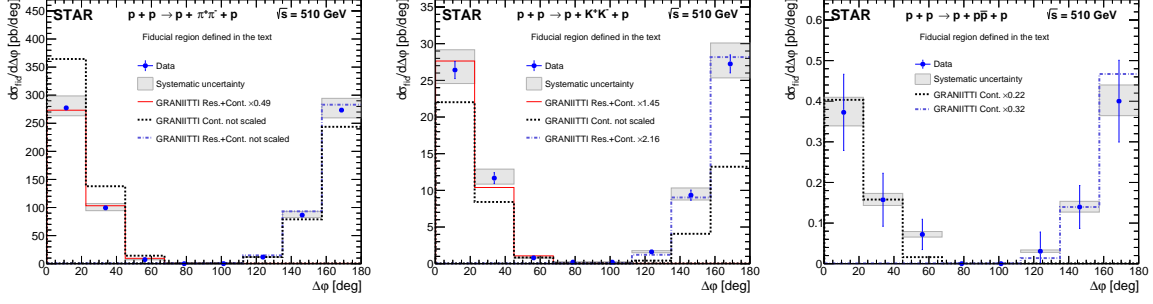
Figure 7. Differential fiducial cross sections of $\pi^+\pi^-$ (left), K^+K^- (middle) and $p\bar{p}$ (right) pairs as a function $\Delta\varphi$ of the forward scattered protons measured in the fiducial volume explained in the text. Data are shown as solid blue points with error bars representing the statistical uncertainties. The systematic uncertainties are shown as gray boxes. The scale uncertainty on the vertical axis due to the effective integrated luminosity is 6.4% and is not shown. Predictions from MC model GRANIITTI are shown separately for each $\Delta\varphi$ region along with the normalization factor.

Particle species	$\Delta\varphi < 90°$ and $\Delta\varphi > 90°$
$\pi^+\pi^-$	$f_0(980)$, $f_2(1270)$, and $f_0(1710)$
K^+K^-	$f_0(980)$, $f_0(1500)$, $f_2(1525)$, and $f_0(1710)$
$p\bar{p}$	only continuum

Table 3. The summary of resonances used in the calculation of GRANIITTI predictions for CEP of $\pi^+\pi^-$, K^+K^-, and $p\bar{p}$ pairs in two regions of the difference in azimuthal angles $\Delta\varphi$ of the forward scattered protons: $\Delta\varphi > 90°$ and $\Delta\varphi < 90°$.

546   In the $\pi^+\pi^-$ invariant mass distribution in both $\Delta\varphi$ regions, expected features seen in
547 previous CEP [2–4] and central production [5] measurements are observed: a sharp drop at
548 about 1 GeV attributed to the quantum mechanical negative interference of $f_0(980)$ with
549 the continuum contribution, and a peak consistent with the $f_2(1270)$. A clear difference
550 between the two $\Delta\varphi$ regions can be seen. In $\Delta\varphi < 90°$, an enhancement at low invariant
551 mass and a suppression of $f_2(1270)$ are observed. Above $m(\pi^+\pi^-) > 1.5$ GeV, there are
552 no significant structures in the cross section, which generally decreases with increasing
553 invariant mass. Evidence of structures at 1.7 and 1.9 GeV in $\Delta\varphi < 90°$ can be seen. The
554 first one can be attributed to $f_0(1710)$ resonance that was considered as a "pure" glueball
555 candidate [33]. Moreover, there is no peak around the mass $m(\pi^+\pi^-) \sim 0.8$ GeV that
556 could be attributed to the $\rho(770)$ meson. Hence, the contributions from photoproduction
557 and Reggeons exchanges should be insignificant.

558   Although GRANIITTI had to be scaled to match the data, the shape with the main
559 features is described quite well. There are few differences: the higher cross section above
560 $m(\pi^+\pi^-) > 1.5$ GeV in $\Delta\varphi > 90°$ and more pronounced $f_0(980)$ resonance in $\Delta\varphi < 90°$.
561 Also, the enhancement at the invariant mass at about 500 MeV could be attributed to the
562 $f_0(500)$ resonance. However, that contribution to the mass spectrum would have to be
563 tuned in GRANIITTI.

564   In the invariant mass of K^+K^- pairs, a strong dependence of differential fiducial cross
565 sections on the azimuthal separation between forward protons ($\Delta\varphi < 90°, \Delta\varphi > 90°$) is
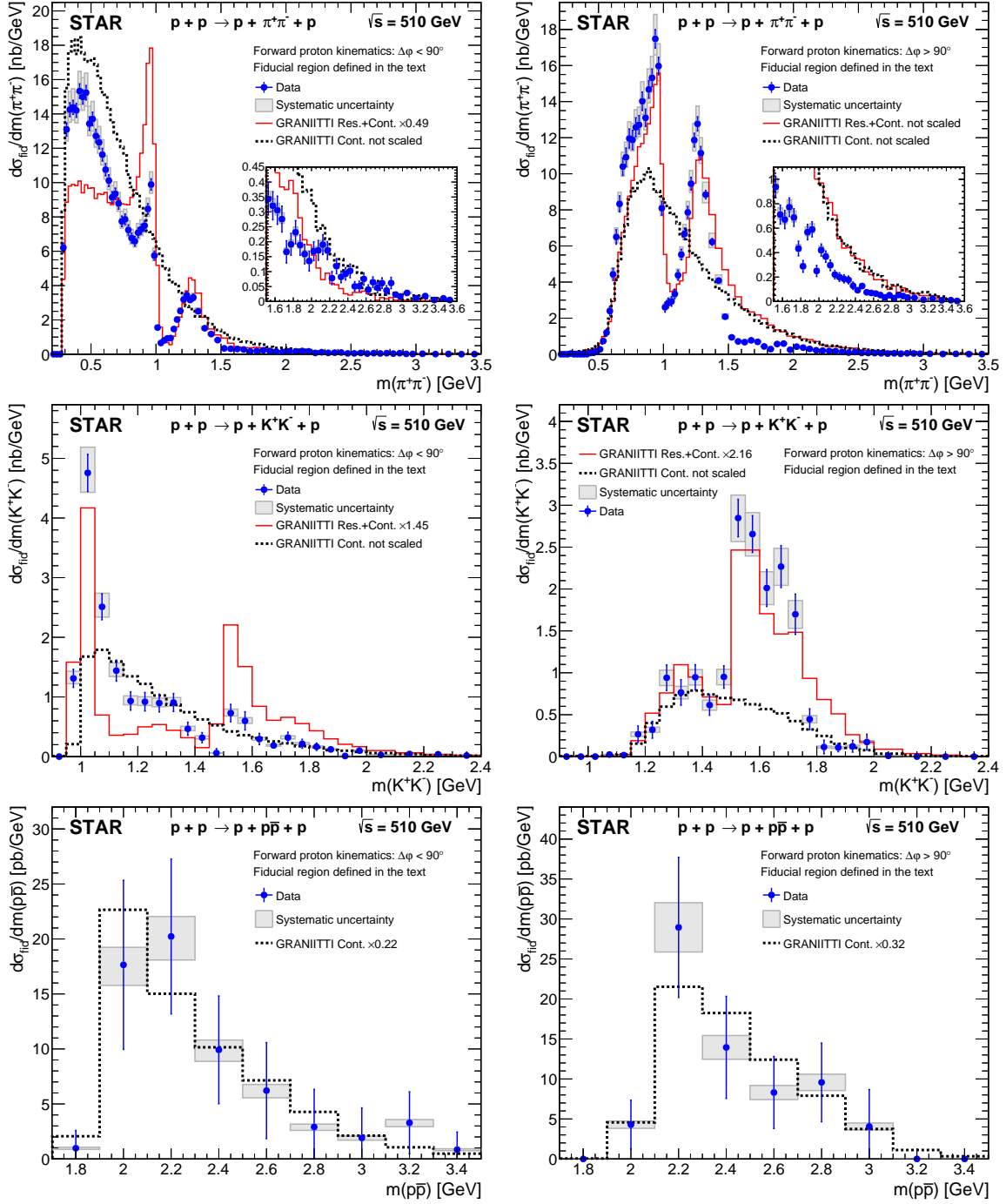
Figure 8. Differential fiducial cross sections of $\pi^+\pi^-$ (top), K^+K^- (middle), and $p\bar{p}$ (bottom) pairs as a function of the invariant mass of the pair in two regions of the difference in azimuthal angles $\Delta\varphi$ of the forward scattered protons: $\Delta\varphi < 90°$ (left) and $\Delta\varphi > 90°$ (right), measured in the fiducial volume explained in the text. Data are shown as solid blue points with error bars representing the statistical uncertainties. The systematic uncertainties are shown as gray boxes. The scale uncertainty on the vertical axis due to the effective integrated luminosity is 6.4% and is not shown. Predictions from MC model GRANIITTI are shown separately for each $\Delta\varphi$ region along with the normalization factor.

observed. In particular, a strong enhancement at low invariant mass in $\Delta\varphi < 90°$. Based on the comparison with GRANIITTI, the enhancement is attributed solely to the $f_0(980)$ resonance contribution.

This is the first observation of $f_0(980)$ production in K^+K^- channel. This is because the experimental setup allows for the detection of states close to the production threshold, particularly in the region of large transverse momentum. The next possible resonance would be $\varphi(1020)$ meson produced via the photoproduction process. However, the contribution from this process is not significant as in the earlier conclusion that photoproduction and Reggeon exchanges are not significant in $\pi^+\pi^-$ channel.

For $\Delta\varphi > 90°$, two structures are seen at about 1.3 and 1.5 GeV. In GRANIITTI, the broad structure around 1.3 GeV is due to the acceptance cut off of the K^+K^- continuum invariant mass distribution at the lower masses, while the peak at $\sim$ 1.5 GeV can be explained by $f_0(1500)$, $f_2(1525)$. There is also a possible peak at $\sim$ 1.7 GeV, which could be due to $f_0(1710)$ resonance. Also a possible enhancement at $m(K^+K^-) \sim 1.975$ GeV is seen.

For $\Delta\varphi < 90°$, peaks at the 1 GeV and 1.5 GeV are seen. They correspond to $f_0(980)$ and ($f_0(1500)$, $f_2(1525)$) resonances. Also, a dip at $m(K^+K^-) \lesssim 1.5$ GeV. The dip can be explained as due the negative interference of $f_0(1500)$ with the continuum production. Also, an enhancement corresponding to $f_0(1710)$ is seen.

Data do not support the presence of the $f_2(1270)$ resonance and GRANIITTI reproduces the invariant mass spectrum quite well without the $f_2(1270)$.

The differential fiducial cross sections of $p\bar{p}$ pairs do not show any significant resonances or any notable $\Delta\varphi$ asymmetry except for a possible dip at $m(p\bar{p}) \sim 3.0$ GeV for $\Delta\varphi < 90°$. Hence, it is compared with the GRANIITTI predictions based solely on continuum contributions. An enhancement at the level of 1σ at $m(p\bar{p}) \sim 2.2$ GeV for $\Delta\varphi > 90°$ is seen. It was also observed at the same level at $\sqrt{s} = 200$ GeV [3].

Figure 9 shows differential fiducial cross sections of $\pi^+\pi^-$, K^+K^-, and $p\bar{p}$ pairs as a function of the pair rapidity in two $\Delta\varphi$ regions. The GRANIITTI predictions are shown as well with the same scaling as in the invariant mass distributions. In general, the shapes of the measured distributions are well described by the GRANIITTI predictions and show the same behavior as at $\sqrt{s} = 200$ GeV [3].

Figure 10 shows differential fiducial cross sections of $\pi^+\pi^-$, K^+K^-, and $p\bar{p}$ pairs as a function of the absolute value of the sum of the squares of the four-momentum transfer of the forward protons ($|t_1 + t_2|$) in two $\Delta\varphi$ regions. GRANIITTI predictions are shown as well. The same scaling as in the invariant mass distributions is applied. The shapes of the measured distributions are strongly affected by the fiducial cuts applied to the forward scattered protons. In general, the shapes are well described by the GRANIITTI predictions in $\Delta\varphi < 90°$ while the distributions in $\Delta\varphi > 90°$ are slightly shifted to the higher values. The shapes are similar to those observed at $\sqrt{s} = 200$ GeV [3].

The large statistics of the $\pi^+\pi^-$ sample enables a more detailed study. The differential fiducial cross sections are studied in three characteristic ranges of the invariant mass of the pair: $m(\pi^+\pi^-) < 1$ GeV, 1 GeV $< m(\pi^+\pi^-) < 1.5$ GeV and $m(\pi^+\pi^-) > 1.5$ GeV. The first
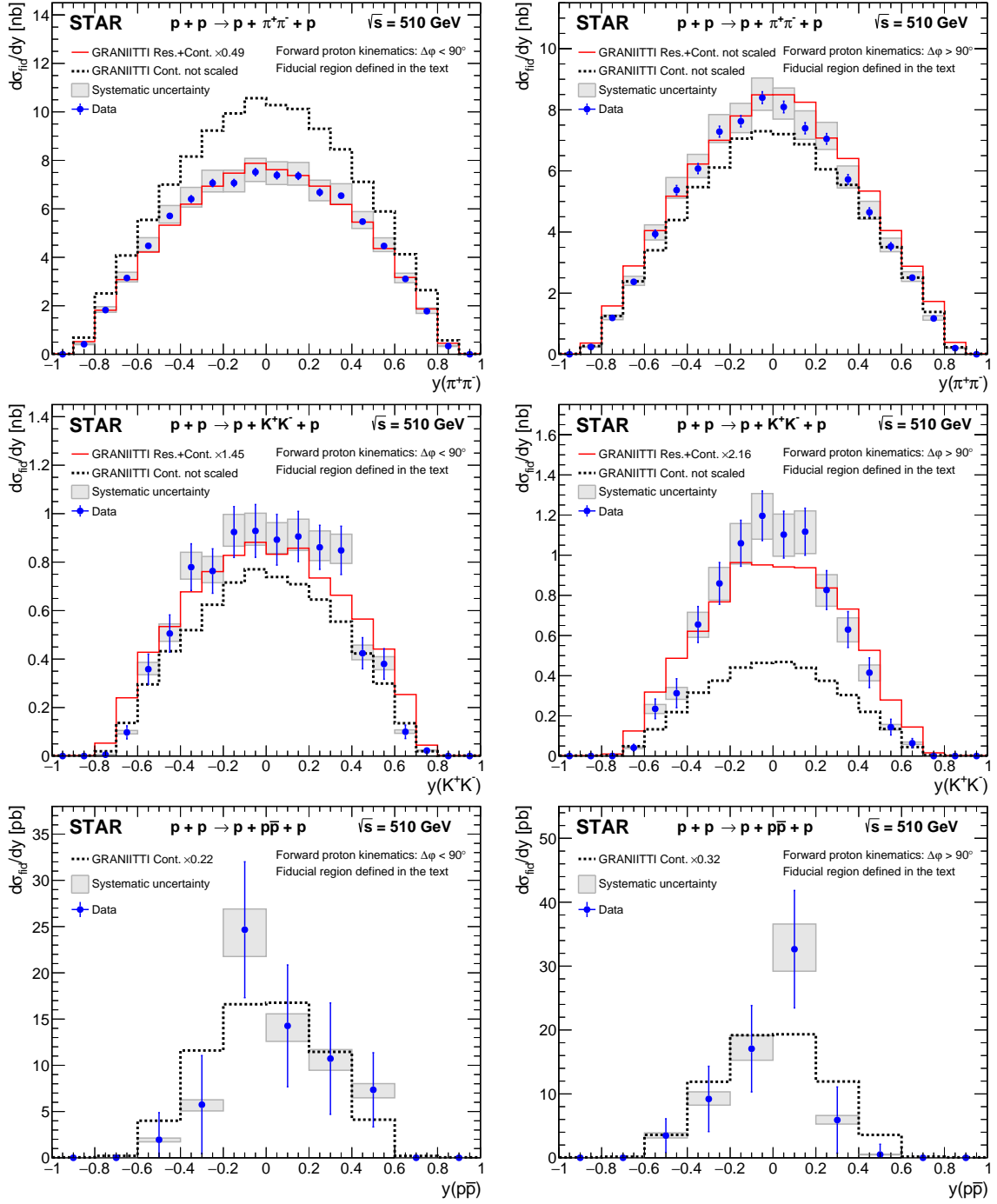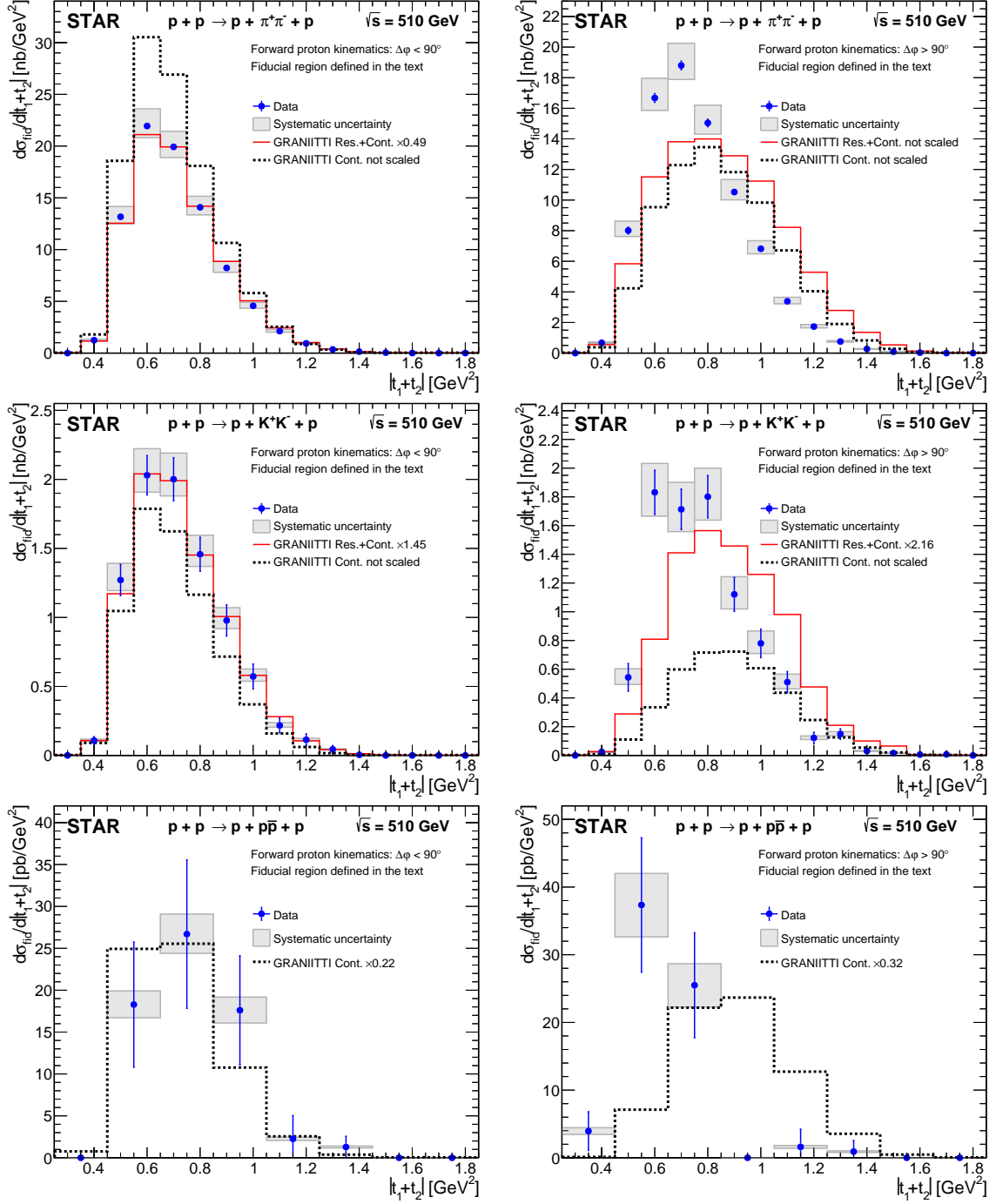
Figure 9. Differential fiducial cross sections of $\pi^+\pi^-$ (top), K^+K^- (middle), and $p\bar{p}$ (bottom) pairs as a function of the pair rapidity in two regions of the difference in azimuthal angles $\Delta\varphi$ of the forward scattered protons: $\Delta\varphi < 90°$ (left) and $\Delta\varphi > 90°$ (right), measured in the fiducial volume explained in the text. Data are shown as solid blue points with error bars representing the statistical uncertainties. The systematic uncertainties are shown as gray boxes. The scale uncertainty on the vertical axis due to the effective integrated luminosity is 6.4% and is not shown. Predictions from MC model GRANIITTI are shown separately for each $\Delta\varphi$ region along with the normalization factor.

Figure 10. Differential fiducial cross sections for CEP of $\pi^+\pi^-$ (top), K^+K^- (middle), and $p\bar{p}$ (bottom) pairs as a function of the absolute value of the sum of the squares of the four-momentum transfer of the forward protons in two regions of the difference in azimuthal angles $\Delta\varphi$ of the forward scattered protons: $\Delta\varphi < 90°$ (left) and $\Delta\varphi > 90°$ (right), measured in the fiducial volume explained in the text. Data are shown as solid blue points with error bars representing the statistical uncertainties. The systematic uncertainties are shown as gray boxes. The scale uncertainty on the vertical axis due to the effective integrated luminosity is 6.4% and is not shown. Predictions from MC model GRANIITTI are shown separately for each $\Delta\varphi$ region along with the normalization factor.

⁶⁰⁸ region is considered to be dominant by continuum production. The second is dominant by
⁶⁰⁹ resonant production, namely by $f_2(1270)$.

⁶¹⁰   Figure 11 shows differential fiducial cross sections of $\pi^+\pi^-$ pairs as a function of the
⁶¹¹ difference in azimuthal angles ($\Delta\varphi$) of the forward scattered protons in three ranges of
⁶¹² the $\pi^+\pi^-$ pair invariant mass. GRANIITTI predictions are shown as well. The strong
⁶¹³ suppression close to $\Delta\varphi = 90°$ is due to the limited azimuthal acceptance in RP detector
⁶¹⁴ system. The differential fiducial cross sections in $\Delta\varphi > 90°$ in the first range of the $\pi^+\pi^-$
⁶¹⁵ pair invariant mass is suppressed due to the to the STAR TPC acceptance. The same
⁶¹⁶ suppression was observed also at $\sqrt{s} = 200$ GeV [3]. In the other ranges, suppressions of
⁶¹⁷ differential fiducial cross sections in $\Delta\varphi < 90°$ are seen. The suppression in the middle
⁶¹⁸ range was also seen at $\sqrt{s} = 200$ GeV [3] and is also predicted by GRANIITTI calculations
⁶¹⁹ assuming only continuum contribution. In the last range, the GRANIITTI predicts the
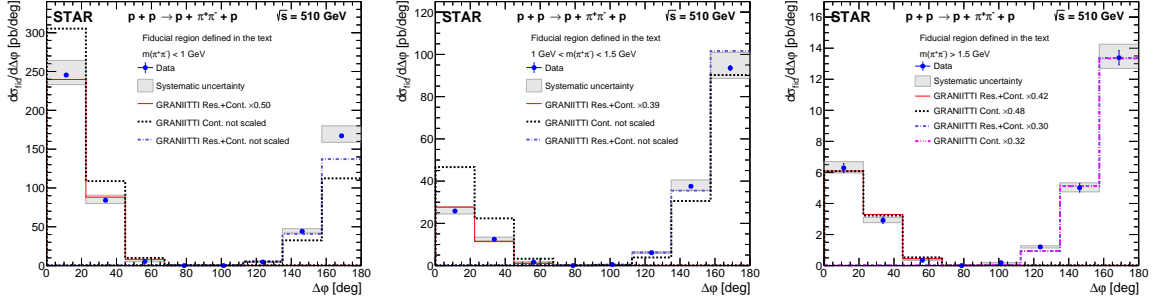⁶²⁰ same asymmetry as seen in the data.

Figure 11. Differential fiducial cross sections of $\pi^+\pi^-$ pairs as a function of the difference in azimuthal angles $\Delta\varphi$ of the forward scattered protons in three ranges of the $\pi^+\pi^-$ pair invariant mass: $m(\pi^+\pi^-) < 1$ GeV (left), 1 GeV $< m(\pi^+\pi^-) < 1.5$ GeV (middle) and $m(\pi^+\pi^-) > 1.5$ GeV (right), measured in the fiducial volume explained in the text. Data are shown as solid blue points with error bars representing the statistical uncertainties. The systematic uncertainties are shown as gray boxes. The scale uncertainty on the vertical axis due to the effective integrated luminosity is 6.4% and is not shown. Predictions from MC model GRANIITTI are shown separately for each $\Delta\varphi$ region along with the normalization factor.

⁶²¹   Figure 12 shows differential fiducial cross sections of hadron $\pi^+\pi^-$ pairs as a function
⁶²² of the pair rapidity in three ranges of the $\pi^+\pi^-$ pair invariant mass and in two $\Delta\varphi$ regions.
⁶²³ GRANIITTI predictions are shown as well. The GRANIITTI predictions describe well the
⁶²⁴ shapes of measured differential fiducial cross sections in both $\Delta\varphi$ regions and in all three
⁶²⁵ ranges of the $\pi^+\pi^-$ pair invariant mass. The measured shapes are similar to those observed
⁶²⁶ at $\sqrt{s} = 200$ GeV [3].
⁶²⁷   Figure 13 shows differential fiducial cross sections of $\pi^+\pi^-$ pairs as a function of $|t_1+t_2|$
⁶²⁸ in three ranges of the $\pi^+\pi^-$ pair invariant mass and in two $\Delta\varphi$ regions. GRANIITTI
⁶²⁹ predictions are shown as well. The GRANIITTI predictions describe well the shapes of
⁶³⁰ measured differential fiducial cross sections in $\Delta\varphi < 90°$ in all three ranges of the $\pi^+\pi^-$
⁶³¹ pair invariant mass. In $\Delta\varphi > 90°$, the GRANIITTI prediction matches the data only
⁶³² for the higher invariant masses while the predictions are shifted to the higher values of
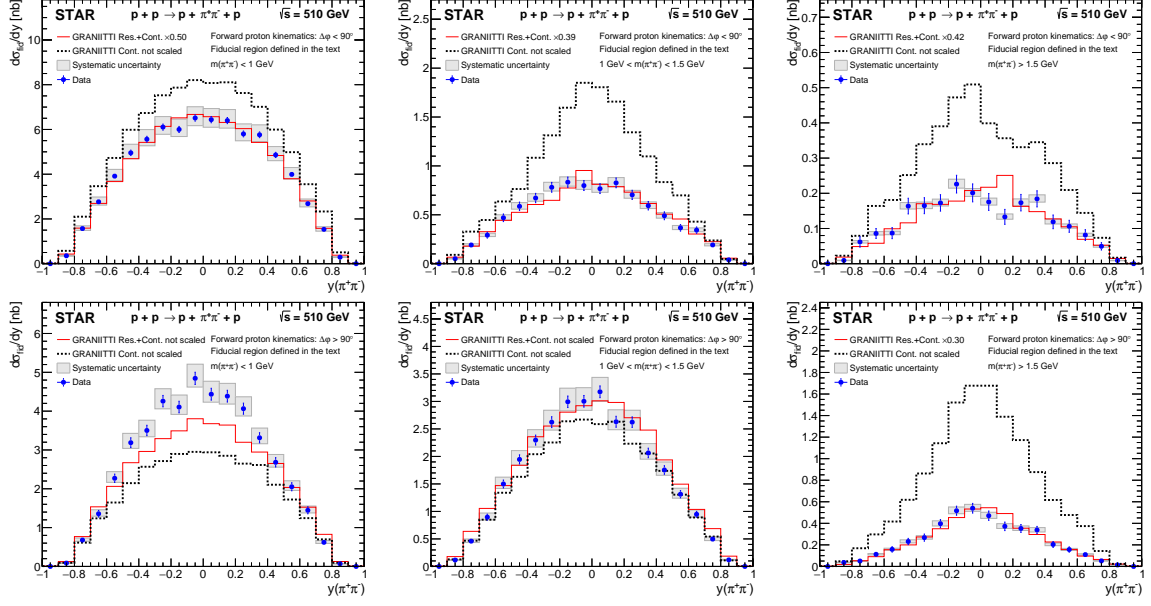⁶³³ $|t_1+t_2|$ for the first two ranges. The measured shapes are comparable to those observed at

Figure 12. Differential fiducial cross sections of $\pi^+\pi^-$ pairs as a function of the pair rapidity in three ranges of the $\pi^+\pi^-$ pair invariant mass: $m(\pi^+\pi^-) < 1$ GeV (left), 1 GeV $< m(\pi^+\pi^-) < 1.5$ GeV (middle) and $m(\pi^+\pi^-) > 1.5$ GeV (right) and into two regions of the difference in azimuthal angles $\Delta\varphi$ of the forward scattered protons: $\Delta\varphi < 90°$ (top) and $\Delta\varphi > 90°$ (bottom), measured in the fiducial volume explained in the text. Data are shown as solid blue points with error bars representing the statistical uncertainties. The systematic uncertainties are shown as gray boxes. The scale uncertainty on the vertical axis due to the effective integrated luminosity is 6.4% and is not shown. Predictions from MC model GRANIITTI are shown separately for each $\Delta\varphi$ region along with the normalization factor.

$\sqrt{s} = 200$ GeV [3]. The higher range of $|t_1 + t_2|$ is due to higher momentum of the forward protons compared to that at $\sqrt{s} = 200$ GeV [3].

8.2 Integrated fiducial cross sections

The integrated fiducial cross sections of $\pi^+\pi^-$, K^+K^-, and $p\bar{p}$ pairs, measured in the fiducial volume explained in the text above, are calculated separately for two regions of the difference in azimuthal angles $\Delta\varphi$ of the forward scattered protons: $\Delta\varphi > 90°$ and $\Delta\varphi < 90°$. The results are presented in Table 4.

9 Summary

We present the results on the CEP of oppositely charged hadron pairs ($\pi^+\pi^-$, K^+K^-, and $p\bar{p}$) in proton-proton collisions at $\sqrt{s} = 510$ GeV with the STAR detector at RHIC. The measurement of forward-scattered protons enabled full control of the process' kinematics and verification of its exclusivity. The measurements are presented within the STAR detector's acceptance, which is determined by the transverse momenta and pseudorapidities of the centrally produced charged hadron pairs, as well as the momenta of forward-scattered protons.
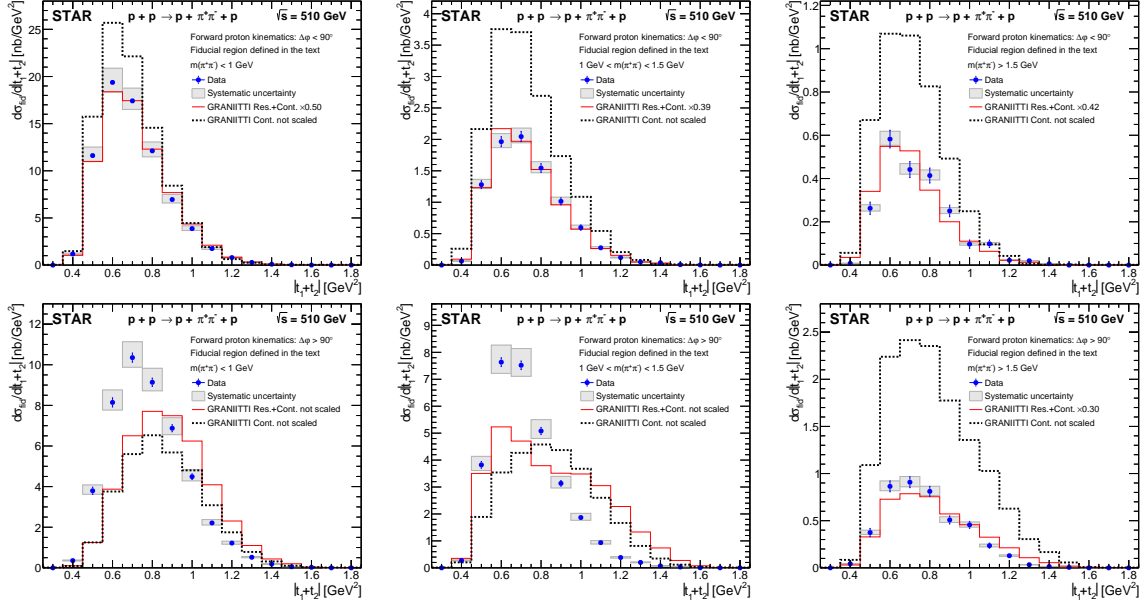
Figure 13. Differential fiducial cross sections of $\pi^+\pi^-$ pairs as a function of the absolute value of the sum of the squares of the four-momentum transfer of the forward protons in three ranges of the $\pi^+\pi^-$ pair invariant mass: $m(\pi^+\pi^-) < 1$ GeV (left), 1 GeV $< m(\pi^+\pi^-) < 1.5$ GeV (middle) and $m(\pi^+\pi^-) > 1.5$ GeV (right) and into two regions of the difference in azimuthal angles $\Delta\varphi$ of the forward scattered protons: $\Delta\varphi < 90°$ (top) and $\Delta\varphi > 90°$ (bottom), measured in the fiducial volume explained in the text. Data are shown as solid blue points with error bars representing the statistical uncertainties. The systematic uncertainties are shown as gray boxes. The scale uncertainty on the vertical axis due to the effective integrated luminosity is 6.4% and is not shown. Predictions from MC model GRANIITTI are shown separately for each $\Delta\varphi$ region along with the normalization factor.

| Particle species | Unit | $\sigma_{\text{fid}} \pm \delta_{\text{stat}} \pm \delta_{\text{syst}}$ | |
		$\Delta\varphi < 90°$	$\Delta\varphi > 90°$
$\pi^+\pi^-$	nb	$8.68 \pm 0.04 \, ^{+0.64}_{-0.43}$	$8.42 \pm 0.04 \, ^{+0.64}_{-0.41}$
K^+K^-	pb	$879 \pm 27 \, ^{+78}_{-57}$	$868 \pm 28 \, ^{+81}_{-84}$
$p\bar{p}$	pb	$13.9 \pm 1.4 \, ^{+0.8}_{-1.3}$	$14.4 \pm 1.5 \, ^{+1.1}_{-1.1}$

Table 4. Integrated fiducial cross sections for CEP of $\pi^+\pi^-$, K^+K^-, and $p\bar{p}$ pairs measured in the fiducial volume explained in the text. Integrated cross sections are presented into two regions of the difference in azimuthal angles $\Delta\varphi$ of the forward scattered protons: $\Delta\varphi > 90°$ and $\Delta\varphi < 90°$. Statistical and systematic uncertainties are provided for each cross section.

The differential fiducial cross sections are presented as a function of the invariant mass, $m(h^+h^-)$, of hadron pairs in two regions of $\Delta\varphi$ the difference between azimuthal angles of the forward-scattered protons. Structures observed in the invariant mass spectra of $\pi^+\pi^-$ and K^+K^- pairs suggest that DIPE is the dominant production mechanism in this fiducial phase space. We observe a strong dependence of the cross section measured here, $d\sigma/dm(h^+h^-)$, on $\Delta\varphi$.

For $\pi^+\pi^-$ pairs, the invariant mass spectrum is consistent with the $f_0(980)$ and $f_2(1270)$ resonances, which have been observed in previous measurements at other collision energies [2–5]. Also, an enhancement consistent with the $f_0(1710)$ is observed.

For K^+K^- pairs, the observed features can be explained as due to the $f_0(980)$, $f_0(1500)$, $f_2(1525)$, and $f_0(1710)$ resonances. Notably, the $f_0(980)$ resonance is observed for the first time in the K^+K^- decay channel, as the experimental setup opened an acceptance of states close to the production threshold at large transverse momentum. The limited statistics do not allow any significant conclusions about the resonances in the $p\bar{p}$ invariant mass spectrum.

We also present the rapidity distributions of the central states and the $|t_1 + t_2|$, and $\Delta\varphi$ distributions of the forward protons. In the $\pi^+\pi^-$ channel, these distributions are presented in three mass regions.

A comparison of the results with predictions from GRANIITTI v1.090 event generator is also presented. In general, GRANIITTI describes the shape of the distributions, but additional scaling factor in the range 0.3 to 1.8 is often needed to match the results. The new data presented here will allow for additional tuning of GRANIITTI and other models of CEP. For example, tuning the contribution from the $f_0(500)$ resonance may improve the agreement between GRANIITTI and the data.

Acknowledgments

References

[1] V. Barone and E. Predazzi, *High-Energy Particle Diffraction*, Springer, Germany (2002).

[2] AXIAL FIELD SPECTROMETER collaboration, *A search for glueballs and a study of double pomeron exchange at the CERN intersecting storage rings*, *Nucl. Phys. B* **264** (1986) 154.

[3] STAR collaboration, *Measurement of the central exclusive production of charged particle pairs in proton-proton collisions at $\sqrt{s} = 200$ GeV with the STAR detector at RHIC*, *JHEP* **2020** (2020) 46.

[4] CMS AND TOTEM collaboration, *Nonresonant central exclusive production of charged-hadron pairs in proton-proton collisions at $\sqrt{s} = 13$ TeV*, *Phys. Rev. D* **109** (2024) 112013.

[5] CDF collaboration, *Measurement of central exclusive $\pi^+\pi^-$ production in $p\bar{p}$ collisions at $\sqrt{s} = 0.9$ and 1.96 TeV at CDF*, *Phys. Rev. D* **91** (2015) 091101.

[6] L.A. Harland-Lang, V.A. Khoze, M.G. Ryskin and W.J. Stirling, *Central exclusive production within the Durham model: a Review*, *Int. J. Mod. Phys. A* **29** (2014) 1430031.

[7] P. Lebiedowicz, et al., *Central exclusive diffractive production of the $\pi^+\pi^-$ continuum, scalar, and tensor resonances in pp and $p\bar{p}$ scattering within the tensor Pomeron approach*, *Phys. Rev. D* **93** (2016) 054015.

[8] C. Ewerz, P. Lebiedowicz, O. Nachtmann and A. Szczurek, *Helicity in proton–proton elastic scattering and the spin structure of the pomeron*, *Phys. Lett. B* **763** (2016) 382.

[9] V.A. Khoze, A.D. Martin and M.G. Ryskin, *Multiple interactions and rapidity gap survival*, *J. Phys. G: Nucl. Part. Phys.* **45** (2018) 053002.

[10] P. Lebiedowicz and A. Szczurek, *Revised model of absorption corrections for the $pp \to pp\pi^+\pi^-$ process*, *Phys. Rev. D* **92** (2015) 054001.

[11] WA91 collaboration, *A further study of the centrally produced $\pi^+\pi^-$ and $\pi^+\pi^-\pi^+\pi^-$ channels in pp interactions at 300 and 450 GeV/c*, *Phys. Lett. B* **353** (1995) 589.

[12] W. Ochs, *The status of glueballs*, *J. Phys. G* **40** (2013) 043001.

[13] M. Harrison, et al., *The RHIC accelerator*, *Annu. Rev. Nucl. Part. Sci.* **52** (2002) 425.

[14] H. Hahn, et al., *The RHIC design overview*, *Nucl. Instrum. Meth. A* **499** (2003) 245.

[15] STAR collaboration, *STAR detector overview*, *Nucl. Instrum. Meth. A* **499** (2003) 624.

[16] STAR collaboration, *The STAR time projection chamber: a unique tool for studying high multiplicity events at RHIC*, *Nucl. Instrum. Meth. A* **499** (2003) 20.

[17] STAR collaboration, *The large-area time-of-flight (TOF) upgrade for the STAR detector*, *AIP Conf. Proc.* **1099** (2009) 778.

[18] STAR collaboration, *The Beam-Beam Counter: a local polarimeter at STAR*, *AIP Conf. Proc.* **2008** (2008) 390.

[19] W. Llope, et al., *The STAR Vertex Position Detector*, *Nucl. Instrum. Methods Phys. Res. A* **759** (2014) 23.

[20] C. Adler, et al., *The RHIC zero degree calorimeters*, *Nucl. Instrum. Meth. A* **470** (2001) 488.

[21] C. Adler, et al., *The RHIC zero-degree calorimeters*, *Nucl. Instrum. Meth. A* **499** (2003) 433.

[22] PP2PP collaboration, *The PP2PP experiment at RHIC: silicon detectors installed in Roman Pots for forward proton detection close to the beam*, *Nucl. Instrum. Meth. A* **535** (2004) 6.

[23] STAR collaboration, *Results on total and elastic cross sections in proton–proton collisions at* $\sqrt{s} = 200$ *GeV*, *Phys. Rev. Lett. B* **808** (2020) 135663.

[24] STAR collaboration, *Results on elastic cross sections in proton–proton collisions at* $\sqrt{s} = 510$ *GeV with the STAR detector at RHIC*, *Phys. Rev. Lett. B* **852** (2024) 138601.

[25] H. Bichsel, *A method to improve tracking and particle identification in TPCs and silicon detectors*, *Nucl. Instrum. Meth. A* **562** (2006) 154.

[26] R. Brun, F. Bruyant, M. Maire, A.C. McPherson and P. Zanarini, *GEANT 3*, CERN, Geneva (1987).

[27] GEANT4 collaboration, *GEANT4—a simulation toolkit*, *Nucl. Instrum. Methods Phys. Res., Sect. A* **506** (2003) 250.

[28] S. van der Meer, *Calibration of the Effective Beam Height in the ISR*, Tech. Rep. CERN-ISR-PO-68-31 (1968).

[29] STAR collaboration, *Measurements of the* Z^0/γ^* *cross section and transverse single spin asymmetry in 510 GeV p+p collisions*, *Phys. Rev. Lett. B* **854** (2024) 138715.

[30] M. Mieskolainen, *GRANIITTI: A Monte Carlo Event Generator for High Energy Diffraction*, 1910.06300.

[31] C. Ewerz, M. Maniatis and O. Nachtmann, *A model for soft high-energy scattering*, *Ann. Phys.* **342** (2014) 31.

[32] M. Mieskolainen, *Graniitti: Towards a Deep Learning-enhanced Monte Carlo Event Generator for High-energy Diffraction*, *Acta Phys. Pol. B Proc. Suppl.* **16** (2023) 6.

[33] S. Dobbs, A. Tomaradze, T. Xiao and K.K. Seth, *Comprehensive study of the radiative decays of* J/ψ *and* $\psi(2S)$ *to pseudoscalar meson pairs, and search for glueballs*, *Phys. Rev. D* **91** (2015) 052006.

753 **The STAR Collaboration**